

---

# EFFECTIVE MEDIUM PROPERTIES OF STEALTHY HYPERUNIFORM PHOTONIC STRUCTURES USING MULTISCALE PHYSICS-INFORMED NEURAL NETWORKS

---

**Roberto Riganti**

Physics Department  
Boston University, Boston

**Yilin Zhu**

Division of Materials Science & Engineering  
Boston University, Boston

**Wei Cai**

Department of Mathematics,  
Southern Methodist University, Dallas

**Salvatore Torquato**

Department of Chemistry, Department of Physics,  
and Princeton Materials Institute  
Princeton University, Princeton

**Luca Dal Negro\***

Department of Electrical & Computer Engineering,  
Division of Materials Science & Engineering,  
Physics Department, and Photonics Center  
Boston University, Boston

\*dalnegro@bu.edu

## ABSTRACT

In this article, we employ multiscale physics-informed neural networks (MscalePINNs) for the inverse retrieval of the effective permittivity and homogenization of finite-size photonic media with stealthy hyperuniform (SHU) disordered geometries. Specifically, we show that MscalePINNs are capable of capturing the fast spatial variations of complex fields scattered by arrays of dielectric nanocylinders arranged according to isotropic SHU point patterns, thus enabling a systematic methodology to inverse retrieve their effective dielectric profiles. Our approach extends the recently developed high-frequency homogenization theory of hyperuniform media and retrieves more general permittivity profiles for applications-relevant finite-size SHU systems, unveiling unique features related to their isotropic nature. In particular, we demonstrate the existence of a transparency region beyond the long-wavelength approximation, enabling effective and isotropic homogenization even without disorder-averaging, in contrast to the case of uncorrelated Poisson random patterns. We believe that the multiscale network approach introduced here enables the efficient inverse design of general effective media and finite-size metamaterials with isotropic electromagnetic responses beyond the limitations of traditional homogenization theories.

**Keywords** Stealthy Hyperuniform · Neural Networks · Homogenization · Multiscale

## 1 Introduction

Hyperuniform states of matter enable scientists to characterize naturally occurring structures such as perfect crystals and quasicrystals, as well as tailored disordered systems. In particular, disordered hyperuniform systems were recently discovered in a variety of contexts and phenomena, including glass formation, spin systems, photonic band structures and radiation engineering, nanophotonics, and biological systems, to name a few [1, 2]. A hyperuniform point pattern is characterized by the vanishing of its structure factor  $S(\mathbf{k})$  when the wavevector goes to zero, resulting in the suppression of long-wavelength density fluctuations. In the context of condensed matter physics, it was shown that two- and three-dimensional systems of particles can freeze into highly degenerate disordered hyperuniform states at zero temperature with stealthy hyperuniform (SHU) point pattern geometry, challenging the traditional belief that liquids freeze into highly symmetric structures [3, 4]. Among the hyperuniform states of matter, SHU systems are characterized by a structure factor that vanishes over a compact interval of wavevectors. Therefore, stealthy hyperuniformity is a stronger condition than standard hyperuniformity because single scattering events are prohibited for a large range of spatial frequencies, thus suppressing the corresponding far-field radiation over sizeable angular ranges. Importantly, the structural correlation properties of disordered SHU media can be largely controlled by the  $\chi$  stealthiness parameter, which equals the ratio of the number of constrained wave vectors in reciprocal space to the total number of degrees of freedom, providing opportunities for tuning the structures in between traditional (uncorrelated) random media for  $\chi = 0\%$  and highly-correlated (periodic) structures for  $\chi = 100\%$ . Moreover, it was established that the degree of short-range order in these systems increases with  $\chi$ , inducing a transition from disordered to crystalline phases when  $\chi > 50\%$  in two spatial dimensions.

Recently, the interaction of hyperuniform media with electromagnetic waves attracted significant interest resulting in novel optical phenomena, such as the discovery of amorphous materials with large, complete, photonic band gaps, photon sub-diffusion and localization, as well as engineering applications to enhanced light absorbers, quantum cascade lasers, directional extractors of incoherent emission from light-emitting diodes, free-form waveguides, Luneburg lenses, and phase/amplitude masks for lensless imaging systems [5, 6, 4, 7, 8, 9]. Moreover, the effective electromagnetic wave properties of stealthy hyperuniform systems have been studied beyond the quasistatic regime within an exact nonlocal theory in the thermodynamic limit of infinite system size, including the prediction of perfect transparency intervals up to finite wavenumbers [10, 11]. This characteristic "transparency regime" is identified by a zero imaginary part of the effective dielectric constant  $\epsilon_e$  within a prescribed range of wavelengths [10, 11]. However, the dynamic homogenization theory cannot be applied to finite-size structures when the strength of the multiple scattering renders the effective permittivity spatially dependent, establishing the need for a more general predictive approach for the inverse design of the effective wave characteristics of disordered hyperuniform media with various engineering applications from photonics and metamaterials to antenna design [12, 13, 14].

In this article, we propose and develop an accurate deep learning methodology for predicting the effective electromagnetic properties of finite-size hyperuniform structures in the dynamic regime based on multiscale physics-informed neural networks (MscalePINNs). Specifically, we apply this approach to disordered SHU and Poisson arrays of dielectric nanopillars of radius  $a$  with constant relative permittivity  $\epsilon_r$  and demonstrate enhanced transparency enabling the accurate inverse retrieval of the effective dielectric permittivity  $\epsilon_r(x, y; k)$  of SHU structures with different sizes and dielectric contrasts. Our results show the inverse retrieval of spatially uniform effective permittivity  $\epsilon_r(x, y; k)$  for the SHU structures without averaging over multiple disorder realizations, in contrast to the case of the uncorrelated Poisson patterns of equivalent density. Moreover, we provide numerical evidence that SHU arrays can be effectively homogenized at shorter wavelengths compared to Poisson arrays with identical particle volume fractions, supporting the conjecture that SHU structures are transparent over a wider range of wavelengths even for finite-size systems. Importantly, we also establish through numerous examples that MscalePINN is a necessary extension of traditional single-scale PINN platforms in situations where significant multiple scattering effects contribute to the retrieval of effective parameters. Finally, by exciting the structures with plane waves at different angles, we show that finite-size SHU arrays feature an isotropic homogenized response, i.e. the retrieved effective parameters do not depend on the

angle of the incoming radiation. In order to present a comprehensive analysis, we vary the size, number of scatterers, stealthiness parameter, incident wavelength, and directions for each investigated structure. Our accompanying Supplementary Material details all the relevant calculation parameters and provides additional comparisons.

## Methods

Since the first system of partial differential equations (PDEs) was introduced by Leonhard Euler in the context of fluid dynamics more than 250 years ago, the numerical approximation of partial differential equations has been driving the progress of science and engineering. In optical science and photonics technology, it is often required to solve differential or integro-differential models governing the scattering and transport of vector waves inside complex and heterogeneous materials or in extended media containing resonant optical nanostructures [15, 16, 17]. While many advanced techniques have been developed for the forward solution of such mathematical problems, the multiscale structure of heterogeneous media generally prevents the accurate and efficient solution of inverse scattering problems of relevance to imaging, acoustics, geophysics, remote sensing, and nondestructive testing. Specifically, in the regime of multiple wave scattering where the transport mean free path  $\xi_t$  is significantly smaller than the system's size  $L$ , the inversion of differential models becomes a nonlinear and computationally intractable problem for traditional numerical techniques. This prevents the accurate prediction of the desired parameters of multi-particle complex structures from a limited set of available field data, motivating the development of alternative and more powerful computational frameworks that leverage learning techniques and optimization methods.

In this context, deep learning inverse design has recently become prevalent in computational science and engineering [18]. When dealing with the ill-posed inverse problems of structurally complex media, it becomes necessary to utilize numerical methods that can fully capture the multiscale nature of the solution in a reasonable amount of time using commercially available processing technologies. Motivated by this need, recent developments in scientific machine learning (ML) introduced physics-informed neural networks (PINNs) as a viable approach to efficiently solve forward and inverse integro-differential problems with minimal computational overhead. Different from standard deep learning approaches, PINNs restrict the space of admissible solutions by enforcing the validity of the PDE models governing the actual physics of the problem. This is achieved by using relatively simple feed-forward neural network architectures as trainable surrogate solutions of the PDEs on the interior and boundary points of their definition domains and leveraging automatic differentiation (AD) techniques readily available in the TensorFlow learning package [19, 20, 21, 22]. Unlike common machine learning algorithms, PINNs are trained on a set of randomly distributed collocation points in order to minimize the PDE residues in a suitable norm [19, 20]. Therefore, PINNs use only one training dataset to obtain the desired solutions, thus relaxing the burdens often imposed by the massive datasets utilized by alternative, i.e. non-physics-constrained, purely data-driven deep learning approaches [23]. Furthermore, PINNs solve highly nonlinear and dispersive inverse and forward problems on the same footing by simply adding an extra loss term to the overall loss function and training over real or synthetic data in order to minimize the residuals for the PDEs and boundary conditions. This feature renders PINNs uniquely effective in solving differential and integro-differential inverse problems with a minimal overhead compared to the corresponding forward problem [24, 25, 26].

Recently, it became apparent in the ML community that deep neural networks (DNNs) learn the low-frequency content of available training data quickly and with a good generalization error, but fail to do so when high-frequency data are involved. This general Fourier principle creates an implicit spectral bias as DNNs preferentially fit training data using low-frequency functions [27, 28, 29, 30, 31]. To solve this issue, the approach of multiscale PINNs (MscalePINNs) was recently introduced to convert the learning and approximation of high-frequency data to that of low-frequency ones, using different sub-networks that learn down-shifted frequency representations of the original datasets and functions [32], as shown below.

To illustrate the approach of the multiscale PINN, we consider a band-limited function  $f(\mathbf{x})$ ,  $\mathbf{x} \in \mathbb{R}^d$ , whose Fourier transform  $\widehat{f}(\mathbf{k})$  has a compact support, i.e.,

$$\text{Supp}\widehat{f}(\mathbf{k}) \subset B(K_{\max}) = \{\mathbf{k} \in \mathbb{R}^d, |\mathbf{k}| \leq K_{\max}\}. \quad (1)$$

We can partition the domain  $B(K_{\max})$  as an union of  $M$  concentric annulus with uniform or non-uniform width, e.g., for the case of uniform width  $K_0$ ,

$$\begin{aligned} A_i &= \{\mathbf{k} \in \mathbb{R}^d, (i-1)K_0 \leq |\mathbf{k}| \leq iK_0\}, \\ K_0 &= K_{\max}/M, \quad 1 \leq i \leq M, \end{aligned} \quad (2)$$

so that

$$B(K_{\max}) = \bigcup_{i=1}^M A_i. \quad (3)$$

As a result, we can decompose the function  $\widehat{f}(\mathbf{k})$  in the Fourier domain as before

$$\widehat{f}(\mathbf{k}) = \sum_{i=1}^M \chi_{A_i}(\mathbf{k}) \widehat{f}(\mathbf{k}) \triangleq \sum_{i=1}^M \widehat{f}_i(\mathbf{k}), \quad (4)$$

and

$$\text{Supp}\widehat{f}_i(\mathbf{k}) \subset A_i. \quad (5)$$

This decomposition in the Fourier space gives a corresponding one in the physical space

$$f(\mathbf{x}) = \sum_{i=1}^M f_i(\mathbf{x}), \quad (6)$$

where

$$f_i(\mathbf{x}) = \mathcal{F}^{-1}[\widehat{f}_i(\mathbf{k})](\mathbf{x}). \quad (7)$$

From (5), we can apply a simple downward scaling to convert the high frequency region  $A_i$  to a low-frequency one. Namely, we define a scaled version of  $\widehat{f}_i(\mathbf{k})$  as

$$\widehat{f}_i^{(\text{scale})}(\mathbf{k}) = \widehat{f}_i(\alpha_i \mathbf{k}), \quad \alpha_i > 1, \quad (8)$$

and, correspondingly, in the physical space

$$f_i^{(\text{scale})}(\mathbf{x}) = \frac{1}{\alpha_i^d} f_i\left(\frac{1}{\alpha_i} \mathbf{x}\right), \quad (9)$$

or

$$f_i(\mathbf{x}) = \alpha_i^d f_i^{(\text{scale})}(\alpha_i \mathbf{x}). \quad (10)$$

So, the spectrum of the scaled function  $\widehat{f}_i^{(\text{scale})}(\mathbf{k})$  is of low frequency if  $\alpha_i$  is chosen large enough, i.e.,

$$\text{Supp}\widehat{f}_i^{(\text{scale})}(\mathbf{k}) \subset \{\mathbf{k} \in \mathbb{R}^d, \frac{(i-1)K_0}{\alpha_i} \leq |\mathbf{k}| \leq \frac{iK_0}{\alpha_i}\}. \quad (11)$$

Now with DNN's preference toward to low-frequency learning, with  $iK_0/\alpha_i$  being small, we can train a DNN  $f_{\theta^{n_i}}(\mathbf{x})$  to learn  $f_i^{(\text{scale})}(\mathbf{x})$  quickly

$$f_i^{(\text{scale})}(\mathbf{x}) \sim f_{\theta^{n_i}}(\mathbf{x}), \quad (12)$$

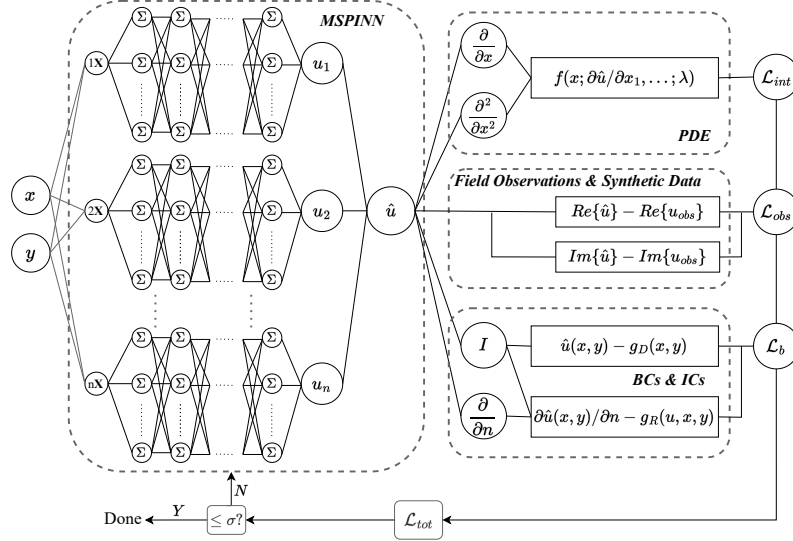


Figure 1: Schematics of the multiscale PINN employed for inverse homogenization of hyperuniform structures.

giving an approximation to  $f_i(\mathbf{x})$  immediately

$$f_i(\mathbf{x}) \sim \alpha_i^d f_{\theta^{n_i}}(\alpha_i \mathbf{x}), \quad (13)$$

and, to  $f(\mathbf{x})$  as well

$$f(\mathbf{x}) \sim \sum_{i=1}^M \alpha_i^d f_{\theta^{n_i}}(\alpha_i \mathbf{x}), \quad (14)$$

giving the format of the MscalePINN [32, 33]. And, the scale factors  $\alpha_i$  can also be converted into trainable parameters to best fit the target functions. In fact, the factor  $\alpha_i^d$  can be absorbed into the weights of the last layer, being linear in most cases, of the sub-neural network  $f_{\theta^{n_i}}(\alpha_i \mathbf{x})$ , the factor  $\alpha_i^d$  outside the sub-neural network can be set to be one to avoid involving large values when  $\alpha_i$  or  $d$  is large without affecting the overall effect of the MscalePINN after training. Each sub-network with scaled inputs can be written as:

$$f_{\theta}(x) = W^{[L-1]} \sigma \circ (\dots (W^{[1]} \sigma \circ (W^{[0]} x + b^{[0]}) + b^{[1]}) \dots) + b^{[L-1]} \quad (15)$$

The general network architecture employed in this article is displayed in Fig. 1. The spatial input parameters  $x, y$  are passed through  $n$  independent sub-networks  $u_i(\alpha_i x, \alpha_i y; \tilde{\theta}_i)$  with different scaling  $\alpha_i$  and hyperparameters  $\tilde{\theta}_i$ . The output of each sub-network  $u_i$  is then combined into the MscalePINNs solution  $\hat{u}(x, y; \tilde{\theta})$  as in Eq. 14 and, through automatic differentiation, is then used to satisfy the PDE, boundary, and initial conditions of the differential equation. Specifically, we consider the following PDE problem with the unknown permittivity distribution  $\epsilon(x, y; k)$ , generally wavevector-dependent, for the surrogate solution  $\hat{u}(x)$  with  $\mathbf{x} = (x_1, \dots, x_d)$  defined on a domain  $\Omega \subset \mathbb{R}^d$ :

$$\varphi \left( \mathbf{x}; \hat{u}, \frac{\partial \hat{u}}{\partial x_1}, \dots, \frac{\partial \hat{u}}{\partial x_d}; \frac{\partial^2 \hat{u}}{\partial x_1^2}, \dots, \frac{\partial^2 \hat{u}}{\partial x_1 \partial x_d}; \dots; \epsilon \right) = 0 \quad (16)$$

The calculated values are then combined into the global loss function  $\mathcal{L}(\tilde{\theta})$ :

$$\mathcal{L}(\tilde{\theta}) = \mathcal{L}_{int}(\tilde{\theta}; \mathcal{N}_{int}) + \mathcal{L}_b(\tilde{\theta}; \mathcal{N}_b) + \mathcal{L}_{inv}(\tilde{\theta}; \mathcal{N}_{inv}) \quad (17)$$

In the loss function above, the component

$$\mathcal{L}_{int}(\tilde{\theta}; \mathcal{N}_{int}) = \frac{1}{|\mathcal{N}_{int}|} \sum_{(x,y) \in \mathcal{N}_{int}} \left\| \varphi \left( x, y; \hat{u}, \frac{\partial \hat{u}}{\partial x}, \frac{\partial \hat{u}}{\partial y}, \dots, \frac{\partial^2 \hat{u}}{\partial y^2}; \epsilon_r \right) \right\|^2 \quad (18)$$

represents the loss term calculated for the PDE in the interior of the domain  $\Omega$  and

$$\mathcal{L}_b(\tilde{\theta}; \mathcal{N}_b) = \frac{1}{|\mathcal{N}_b|} \sum_{(x,y) \in \mathcal{N}_b} \|\mathcal{B}(\hat{u}, x, y)\|^2 \quad (19)$$

is the loss term for the boundary conditions of the PDE, where  $(x, y) \in \partial\Omega$ . Finally, in order to solve general inverse electromagnetic problems, we introduce

$$\mathcal{L}_{inv}(\tilde{\theta}; \mathcal{N}_{inv}) = \frac{1}{|\mathcal{N}_{inv}|} \sum_{(x,y) \in \mathcal{N}_{inv}} \left( \|\text{Re}[\hat{u}(x, y)] - \text{Re}[u_{obs}(x, y)]\|^2 + \|\text{Im}[\hat{u}(x, y)] - \text{Im}[u_{obs}(x, y)]\|^2 \right) \quad (20)$$

as the inverse loss term calculated on the real and imaginary parts of a complex field obtained through numerical simulations, and  $\mathcal{N}_{int}$ ,  $\mathcal{N}_b$ ,  $\mathcal{N}_{inv}$  are the number of residual points for each loss term. In this article, we deal with electromagnetic homogenization problems for which we use the Helmholtz equation to constrain MscalePINNs and retrieve effective homogenized model parameters. In particular, we use the the complex Helmholtz equation for inhomogeneous two-dimensional effective media under TM polarization excitation:

$$\nabla^2 E_z(x, y) + \epsilon_r(x, y; k) k_0^2 E_z = 0 \quad (21)$$

where  $E_z$  is the z-component of the electric field,  $k_0 = \frac{2\pi}{\lambda}$  is the wavenumber in free space, and  $\epsilon_r(x, y; k)$  is the relative permittivity of the non-homogeneous effective medium (spatially dependent), which is almost constant in the case of a homogenized effective medium. Because  $E_z$  and  $\epsilon_r(x, y; k)$  are complex variables, separating Eq. 21 into real and imaginary parts yields:

$$\begin{aligned} \nabla^2 \text{Re}[E_z](x, y) &= -\text{Re}[E_z] \text{Re}[\epsilon_r(x, y; k)] + \text{Im}[E_z] \text{Im}[\epsilon_r(x, y; k)] k_0^2 \\ \nabla^2 \text{Im}[E_z](x, y) &= -\text{Im}[E_z] \text{Re}[\epsilon_r(x, y; k)] - \text{Re}[E_z] \text{Im}[\epsilon_r(x, y; k)] k_0^2 \end{aligned} \quad (22)$$

The loss term in Eq. 18 includes both terms above evaluated on the interior of the domain. In order to achieve the homogenization of the investigated scattering arrays we inversely retrieved the effective permittivity parameter  $\epsilon_r(x, y; k)$  of the Helmholtz equation by training the MscalePINNs over a synthetic dataset composed of complex field values. In particular, we performed finite element method (FEM) simulations of the total complex electric field using COMSOL Multiphysics<sup>TM</sup> [34] and utilized the resulting data set to retrieve the effective electric permittivity profile  $\hat{\epsilon}(x, y; k)$  represented by its own neural network following the methodology introduced in references [24, 25]. Throughout this paper, we will employ different MscalePINN architectures depending on the problem, and for this reason, we have included Table S1 in the Supplementary Material that lists all the relevant network hyperparameters employed in our study. All the codes were developed in-house using TensorFlow [35] and numerical simulations were performed using, depending on the problem, different types of GPUs, i.e., we employed either an NVIDIA P100, NVIDIA V100, or NVIDIA A40.

We begin our study by retrieving the homogenized complex permittivity of a stealthy hyperuniform array of diameter  $L = 10\mu\text{m}$  composed of  $N = 396$  dielectric nanocylinders of radius  $a = 125\text{nm}$ , displayed in Fig. 2(a). The corresponding structure factor  $S(\mathbf{k})$  is shown in Figure S2. For this example, we used  $\chi = 0.5$ ,  $\epsilon_r = 3.0$ ,  $\langle d \rangle / \lambda = 0.15$ , and  $\phi = 0.2$ , where  $\phi = \rho v(a)$  is the particle volume fraction at number density  $\rho$  and sphere volume  $v(a)$ , and  $\langle d \rangle$  is the average first-neighbor distance of the pillars in the array. The MscalePINNs utilized to solve this inverse homogenization problem is a 4-scale MscalePINNs with 4 layer, each with 64 neurons, and it is trained on the real and imaginary parts of the total electric field considering the excitation wavelength  $\lambda = 3.0\mu\text{m}$ .

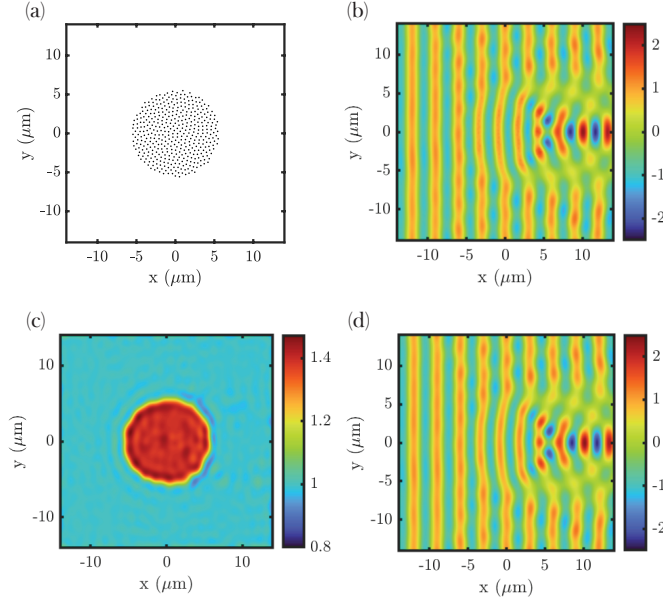


Figure 2: (a) SHU array of 396 particles,  $\chi = 0.5$ ,  $\epsilon_r = 3.0$ ,  $\langle d \rangle / \lambda = 0.15$  employed for the MscalePINNs homogenization validation. (b) The real part of the FEM electric field inverse train dataset is employed to train MscalePINNs to homogenize panel (a). The incident plane wave wavelength is  $\lambda = 3.0 \mu\text{m}$ . (c) MscalePINN's predicted relative permittivity distribution, which is then used to perform a forward COMSOL simulation displayed in panel (d) to compare with the "true" field used in training.

Table 1: Comparison of the real part of the homogenized effective permittivity  $\hat{\epsilon}(x, y; k)$  between the ensemble average and single realization for SHU and Poisson structures with the same size.

Structure	Calculation	$\langle \text{Re}[\hat{\epsilon}(x, y; k)] \rangle$	$\sigma\{\langle \text{Re}[\hat{\epsilon}(x, y; k)] \rangle\}$
SHU	Single realization	1.391	2.8%
	Ensemble average	1.404	1.9%
Poisson	Single realization	1.412	8.8%
	Ensemble average	1.413	3.4%

In Fig. 2(b) we display the real part of the electric field distribution used during training. The effective permittivity profile  $\hat{\epsilon}(x, y; k)$  retrieved by MscalePINNs for a single realization of the investigated SHU array is displayed in panel (c). Remarkably, the effective permittivity is well-localized within the geometrical support of the array with a spatially uniform distribution quantified by the average value of  $\langle \text{Re}[\hat{\epsilon}(x, y; k)] \rangle = 1.39 \pm 2.8\%$ . To better characterize the retrieved homogeneous permittivity profile in the static regime we also calculated the effective medium theory prediction using the Bruggeman mixing formula valid for the bulk case [36]:

$$\sum_i f_i \frac{\epsilon_i - \epsilon_e}{\epsilon_i + \epsilon_e} = 0 \quad (23)$$

where  $\epsilon_e$  is the effective permittivity,  $f_i$  is the filling fraction, and  $\epsilon_i$  is the permittivity of the  $i$ -th component. For a two-phase system under TM polarized incident radiation, Eq. 23 reduces to [11]:

$$\epsilon_{brugg} = f_1 \epsilon_1 + f_2 \epsilon_2 \quad (24)$$

For the system studied in Fig. 2(c),  $\epsilon_{brugg} = 1.4$ , differing only by 0.6% from MscalePINNs and within the uncertainty range predicted. In Fig. 2(d) we display the real part of the total electric field obtained via a forward FEM calculation

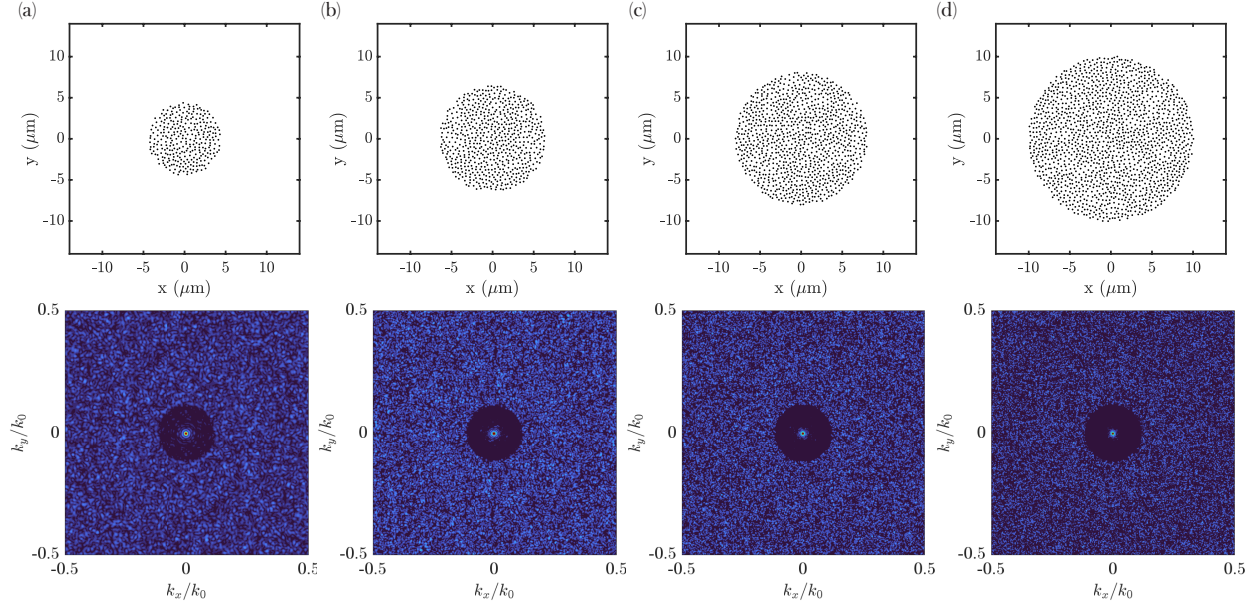


Figure 3:  $S(\mathbf{k})$  plot of four  $\chi = 0.3$  SHU structures with  $N = 299, 633, 1002,$  and  $1553$ , respectively. This figure shows that, even for  $N \approx 300$ , the stealthy patterns are evident.

performed using the retrieved permittivity profile from panel (c), which is then used to calculate the  $L^2$  error including both the real and imaginary part of the training field. The obtained complex field error in the retrieval of the permittivity parameter was found to be 1.1%, demonstrating the high accuracy of the solution achieved by the developed MscalePINNs.

To further investigate the quality of the reconstruction, we also performed an ensemble average of 10 different SHU arrays configurations all generated with the same stealthiness parameter  $\chi = 0.5$ ,  $\epsilon_r = 3.0$ , and  $N = 395 \pm 5$  and with constant particle volume fraction  $\phi = 0.2$ . Our results are summarized in the first row of Table 1 which displays almost identical results to the single realization case when point-wise spatial averaging is performed over the SHU realizations. As a comparison, we also show in Table 1 the results of the same ensemble averaging analysis performed on 10 different realizations of Poisson uncorrelated random (UR) structures with  $\epsilon_r = 3.0$ ,  $N = 395 \pm 5$ , and  $\phi = 0.2$ . We note that, compared to the SHU configuration, the single realization for the Poisson structure features a significant inhomogeneity in the spatial distribution of  $\langle \text{Re}[\hat{\epsilon}(x, y; k)] \rangle$  due to larger fluctuations among the different disorder realizations. However, we note that even in this case the retrieved effective medium permittivity for the Poisson point pattern has an  $L^2$  error lower than 5% when the forward scattered FEM field of the array was compared to the one obtained from the inversely retrieved permittivity. This indicated that MscalePINNs retrieved an accurate spatially dependent permittivity, i.e., an inhomogeneous effective medium, but this case cannot be homogenized using a classical mixing approach for the bulk. Consistently, when performing the ensemble average and point-wise spatial average to retrieve  $\langle \text{Re}[\hat{\epsilon}(x, y; k)] \rangle$  for the Poisson structure, we notice that the obtained value of  $\langle \text{Re}[\hat{\epsilon}(x, y; k)] \rangle = 1.413$  is still larger than both the single realization and ensemble average value of the SHU structure  $\langle \text{Re}[\hat{\epsilon}(x, y; k)] \rangle_{ens} = 1.404$ , which agrees almost perfectly with the Bruggeman prediction of 1.4. Therefore, we conclude that MscalePINNs retrieved an accurate field distribution and  $\epsilon_r(x, y)$  for both the SHU and Poisson arrays, but that a homogeneous permittivity can only be achieved for the SHU structures due to their significantly larger degree of spatial uniformity.

### Transparency of finite-size structures

Recent work by Torquato and Kim [10, 11] led to an exact non-local strong-contrast expansion of the effective dynamic dielectric tensor  $\epsilon(x, y)$  in the thermodynamic limit [10], and more recently they extended these results beyond the long-

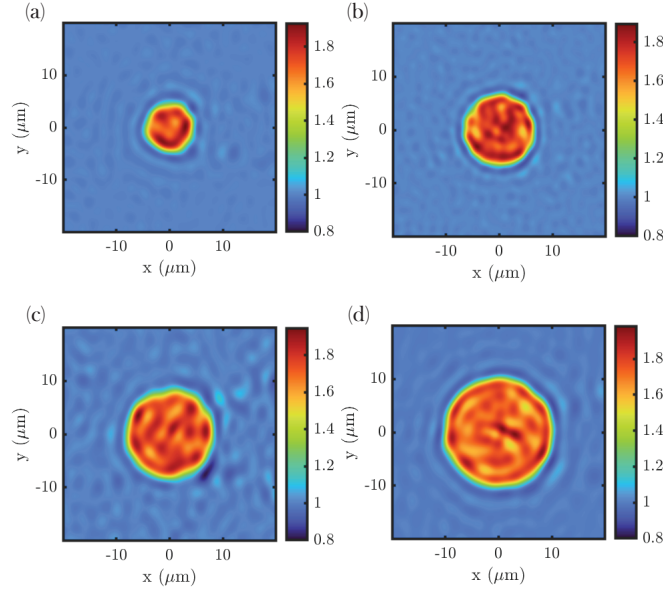


Figure 4: (a)-(d) Scaling analysis of the retrieved effective medium performed on four SHU arrays with 299, 633, 1002, and 1553 particles, respectively, and  $\langle d \rangle / \lambda = 0.06$ . The average of MscalePINNs’s permittivity profile displayed in the four panels all have a computed average value within the region of  $\langle \text{Re}[\hat{\epsilon}(x, y; k)] \rangle = 1.70 \pm 5.9\%$ , independently of the size of the hyperuniform array.

wavelength regime for layered and transversely isotropic media [11]. Their work provides an analytical prediction for the wavelength range in which SHU structures achieve perfect transparency or, equivalently, for the wavelength regime where the effective dielectric constant has a zero imaginary part. However, to the best of our knowledge, no previous work has established if this transparency prediction is modified by finite-size arrays. In order to address this open question we performed a study over several SHU arrays with different sizes and numbers of pillars  $N = 299, 633, 1002,$  and  $1553$ . We also computed the structure factors for the corresponding point patterns and displayed the results in Fig. 3. Interestingly, we note that characteristic stealthy hyperuniform behavior begins to manifest itself already at relatively small  $N$ .

In Fig. 4 we display the retrieved effective permittivity  $\hat{\epsilon}(x, y; k)$  for the four stealthy hyperuniform structures shown in Fig. 3. The simulations the parameters  $\chi = 0.3$ ,  $\epsilon_r = 4.0$ , and  $\phi = 0.25$  were kept constant for all the arrays in order to compare with the theoretical predictions for the infinite bulk limit shown in Ref. [11]. We train a 4-scale MscalePINNs with 2 layers and 64 neurons each using FEM computed forward fields at plane wave excitation wavelength  $\lambda = 6.28\mu\text{m}$ , corresponding to the regime of perfect transparency predicted by Torquato et al. [11]. We display the real part of the retrieved permittivity profiles  $\hat{\epsilon}(x, y; k)$  in order of increasing array size in Fig. 4(a)-(d), and compute the mean and standard deviation inside of the array region. The average of the retrieved effective dielectric function for the four structures is  $\langle \text{Re}[\hat{\epsilon}(x, y; k)] \rangle = 1.7 \pm 5.9\%$  and  $\langle \text{Im}[\hat{\epsilon}(x, y; k)] \rangle = 10^{-4}$ , independent of the array size. This result is extremely close to the predicted value in Ref. [11] for transversely isotropic media with  $\chi = 0.3$ ,  $\epsilon_r = 4.0$ , and  $\phi = 0.25$ . Therefore, from this analysis, we conclude that finite-size scaling does not perturb appreciably the value of the retrieved dielectric constant of SHU arrays. In the next section, we investigate the homogenization behavior at shorter wavelengths for the SHU structures and the uncorrelated Poisson arrays.

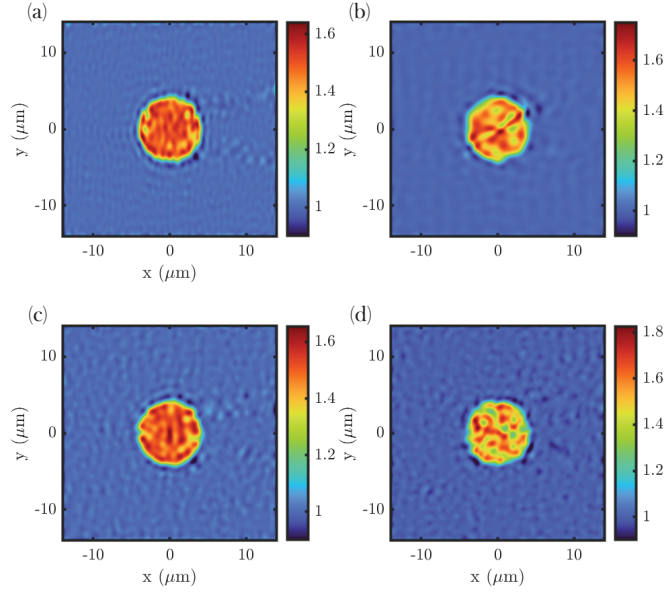


Figure 5: (a) and (b) Comparison between the retrieved permittivity profile  $\langle \text{Re}[\hat{\epsilon}(x, y; k)] \rangle$  of a stealthy hyperuniform array with  $\chi = 0.3$ ,  $N = 663$  particles and the inhomogeneous effective medium of a Poisson array of  $N = 663$  particles. The inverse scattered field used in training had  $\lambda = 2.09\mu\text{m}$  ( $\langle d \rangle / \lambda = 0.1$ ), or  $k_0 = 3.0\mu\text{m}^{-1}$ . (c) and (d) Comparison of the same structures used in panels (a) and (b) but with lower wavelength of the incident scattering field,  $\lambda = 1.59\mu\text{m}$  ( $\langle d \rangle / \lambda = 0.14$ ), or  $k_0 = 4.0\mu\text{m}^{-1}$ . Already at  $\lambda = 1.59\mu\text{m}$ , the Poisson array displays evident losses and homogenization cannot be achieved.

### Comparison with Poisson point patterns

To compare the homogenization behavior of SHU and Poisson structures we consider two arrays with  $N \approx 660$  dielectric nanocylinders of radius  $a = 67.5$  nm, packing fraction  $\phi = 0.16$ , and diameter  $L = 8\mu\text{m}$ . Their structure factors  $S(\mathbf{k})$  plots are plotted in Figure S2. Fig. 5(a) and (c) show the MscalePINNs's homogenized  $\epsilon_r(x, y)$  for  $\lambda = 2.09\mu\text{m}$  and  $\lambda = 1.57\mu\text{m}$ , respectively, for the SHU structure with  $\chi = 0.3$  and  $\epsilon_r = 4.0$ . In this study, the choice of wavelengths for the simulation was informed by Torquato's calculation of the predicted region of transparency for a SHU array. Therefore, we consider here the scattering radiation well beyond the long-wavelength approximation regime and we refer to the criterion specified by the inequality below that characterizes the full extent of the predicted transparency region [11]:

$$k_0 \rho^{-1/2} = 2\pi \frac{\langle d \rangle}{\lambda} \lesssim 1.5, \quad \rho = \frac{N}{\pi R^2} \quad (25)$$

where  $R$  is the radius of the SHU array. For the structures considered in this example, the inequality 25 can be solved for the  $k_0$  value up to which the theoretical predictions are accurate, yielding  $k_0 \approx 5.5\mu\text{m}^{-1}$ . Figure 5 displays the inverse homogenization of SHU and Poisson arrays under incident radiation of  $k_0 = 3.0\mu\text{m}^{-1}$ ,  $4.0\mu\text{m}^{-1}$ , or  $\lambda = 2.09\mu\text{m}$  and  $1.57\mu\text{m}$ , respectively. In panels (a) and (c), both solutions are properly homogenized, with  $\langle \text{Re}[\hat{\epsilon}(x, y; k)] \rangle = 1.48 \pm 4\%$  and  $\langle \text{Im}[\hat{\epsilon}(x, y; k)] \rangle = 10^{-3} \approx 0$  for  $\lambda = 2.09\mu\text{m}$  and  $\langle \text{Re}[\hat{\epsilon}(x, y; k)] \rangle = 1.492 \pm 4.7\%$  and  $\langle \text{Im}[\hat{\epsilon}(x, y; k)] \rangle = 10^{-5} \approx 0$  for  $\lambda = 1.57\mu\text{m}$ . Therefore, the calculations performed with MscalePINNs confirmed the theoretical prediction of transparency even for the finite-size structure.

For the Poisson structures, however, the homogenization fails already at wavelengths away from the SHU critical value of  $5.5\mu\text{m}^{-1}$ . Fig. 5(b) shows the inhomogeneous profile of the real part of the effective permittivity profile  $\hat{\epsilon}(x, y; k)$  predicted by the MscalePINNs for  $\lambda = 2.09\mu\text{m}$ . For this inhomogeneous effective medium,  $\langle \text{Re}[\hat{\epsilon}(x, y; k)] \rangle =$

$1.49 \pm 6.8\%$ , but MscalePINNs failed to retrieve the imaginary component of  $\hat{\epsilon}(x, y; k)$ , despite an  $L^2$  error on the FEM validation of 4%. The inability to retrieve a homogenized effective permittivity is even more apparent at lower wavelengths, where for  $\lambda = 1.57\mu\text{m}$  the MscalePINN correctly predicts an effective permittivity profile  $\hat{\epsilon}(x, y; k)$  with  $\langle \text{Re}[\hat{\epsilon}(x, y; k)] \rangle = 1.5 \pm 12\%$  shown in Fig. 5(d), but fails to predict the imaginary component of  $\hat{\epsilon}(x, y; k)$ . This evident failure to homogenize the random point pattern for  $\lambda = 2.09\mu\text{m}$  and  $1.57\mu\text{m}$  compared to the SHU structure is both qualitative and quantitative. In fact, the spatial non-uniformity of  $\langle \text{Re}[\hat{\epsilon}(x, y; k)] \rangle$  for the Poisson structure, measured by the associated standard deviation  $\sigma$ , is almost an order of magnitude greater than that of the SHU structure for the same incoming wavelength. In Fig. 6 we display this situation by showing the spread of the real part of  $\hat{\epsilon}(x, y; k)$  retrieved by MscalePINNs for the same structures from Fig. 5 with additional  $k$ -vectors values  $k_0$  denoting simulations conducted at different wavelengths, including  $k_0 = 1.0, 2.0\mu\text{m}^{-1}$  for both the Poisson and SHU structure, and  $k_0 = 5.0, 5.5\mu\text{m}^{-1}$  for only the SHU. The investigated range of wavenumber  $k_0$  corresponds to a ratio of  $\langle d \rangle / \lambda = 0.034$  for the longest wavelength and  $\langle d \rangle / \lambda = 0.19$  for the shortest wavelength. All the FEM training fields and  $\langle \text{Re}[\hat{\epsilon}(x, y; k)] \rangle$  plots for each  $k$ -value considered here for both the SHU and Poisson structures can be found in the Supplementary Information S3 and S4, respectively. Each simulation was performed on both structures with identical network architectures. However, despite achieving high accuracy for both structures at  $k$ -values below and including  $4.0\mu\text{m}^{-1}$ , the MscalePINNs failed to retrieve a localized effective medium for the Poisson structures at higher  $k$ -vectors. In contrast, MscalePINNs retrieved a highly accurate homogenized  $\hat{\epsilon}(x, y; k)$  until the predicted threshold for SHU structures of  $k_0 \approx 5.5\mu\text{m}^{-1}$ , with an  $L^2$  error of 6%. Beyond this value, MscalePINNs could not retrieve an effective medium anymore for the SHU arrays as well. In Fig. 6 we have included the MscalePINN's prediction on the single realization beyond the  $k_0$  critical value in the grey shaded region, where the  $L^2$  error was much higher with a value of 24%. We also note that for the SHU array, the real part of  $\hat{\epsilon}(x, y; k)$  becomes less and less homogeneous as we approach the edge of the predicted transparency region. In this case, the MscalePINN continues to accurately retrieve an effective, albeit inhomogeneous, medium until the predicted edge of  $k_0 = 5.5\mu\text{m}^{-1}$ . This drastic difference in the expressive power of identical MscalePINN architectures when dealing with the homogenization and inverse permittivity parameter retrieval of Poisson and SHU structures fully supports the conclusion that SHU structures can be more easily homogenized than traditional random media and their homogenization eventually fails only at higher  $k$  vectors than their Poisson counterparts.

To conclude our analysis, we have also included in Supplementary Information S5 a comparison between the MscalePINN and single-scale PINN homogenization profiles at high  $k$  values for the SHU structures. This comparison supports the conclusion that MscalePINN is necessary when solving electromagnetic transport problems for the strength of multiple scattering considered here. The additional plots displayed in the Supplementary Information show that the best single-scale PINN training completely fails to capture the multiscale field variations intrinsic to the nature of this problem for  $k$  values close to the SHU  $k$ -space transparency edge, whereas MscalePINN accurately retrieves a well-localized homogeneous medium constant. Therefore, we established through numerous examples that MscalePINN is a powerful extension of traditional single-scale PINN architectures that becomes necessary when dealing with significant multiple scattering contributions. In the final section below, we conclude our analysis by additionally demonstrating that homogenized SHU structures feature isotropic homogenized responses that are highly desired characteristics for the engineering of angle-insensitive effective media.

### Angular independence

To demonstrate numerically that homogenized stealthy hyperuniform arrays are isotropic with respect to the incoming scattering electric field, we perform angle-dependent simulations on a stealthy hyperuniform array  $N = 236$  with  $\chi = 0.5$ ,  $\epsilon_r = 3.0$ , and  $\phi = 0.20$ . In Fig. 7(a) we display the SHU array with the angles employed to generate the forward FEM numerical simulations utilized to train the 4-scale MscalePINNs with 4 layers by 64 neurons each. As in the previous studies, we have included the corresponding structure factor  $S(\mathbf{k})$  in the Supporting Information Figure S6, together with the inverse training FEM fields displayed in Figure S7. The predicted homogenized permittivity

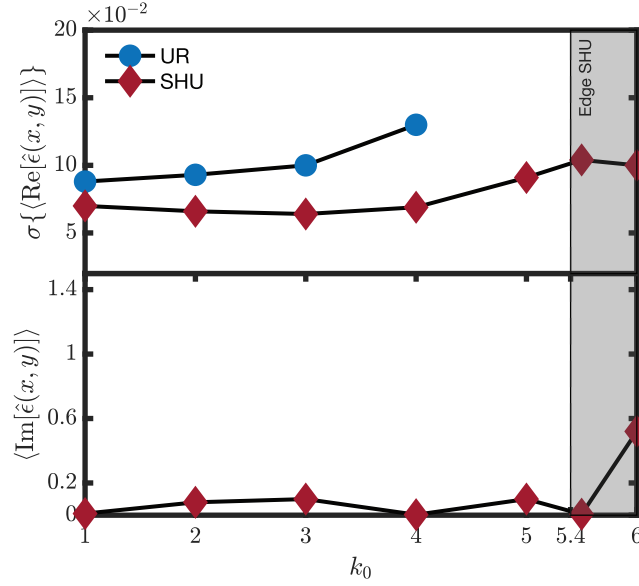


Figure 6: Comparison of the measure of inhomogeneity  $\epsilon_r(x, y)$  retrieved by MscalePINNs for the Poisson and stealthy hyperuniform structure displayed in Fig. 5.  $\sigma\{\langle \text{Re}[\hat{\epsilon}(x, y; k)] \rangle\}$  for the SHU is constant and lower than that of the Poisson structure for the same wavelength range, and it only begins to increase when the incoming field  $k_0$  vector approaches the threshold value of  $k_0 \approx 5.5 \mu\text{m}^{-1}$ . MscalePINNs cannot retrieve an effective  $\epsilon_r(x, y)$  for  $k_0$  greater than  $4.0 \mu\text{m}^{-1}$ . Meanwhile, for all the  $k$ -values below the threshold value,  $\langle \text{Im}[\hat{\epsilon}(x, y; k)] \rangle \approx 0$  for the SHU array, as theoretically predicted.

profiles  $\epsilon_r(x, y)$  are shown in Fig. 7(b)-(d), displaying the MscalePINNs precision in capturing contour features on the boundary of the hyperuniform array. All three permittivity profiles present an accurate agreement in the real and imaginary part of  $\epsilon_r(x, y)$ , with  $\langle \text{Re}[\hat{\epsilon}(x, y; k)] \rangle = 1.28 \pm 3\%$  and  $\langle \text{Im}[\hat{\epsilon}(x, y; k)] \rangle = 10^{-4} \approx 0$ . To confirm that the three homogenized effective media have indeed the same electromagnetic response, we selected the homogenized permittivity profile  $\epsilon_r(x, y)$  trained with the incoming radiation at  $\theta = 0^\circ$  and performed two forward FEM simulations at  $\theta = 45^\circ$  and  $-30^\circ$ . We then computed an  $L^2$  error between the forward field used in training on the SHU array at  $\theta = 45^\circ$  and  $-30^\circ$  and the one just recomputed by utilizing the homogenized structure trained with the incoming radiation at  $\theta = 0^\circ$ . The two  $L^2$  errors were 1.2% and 2.4%, respectively, showing that the effective medium retrieved by MscalePINNs when trained with incoming radiation at  $\theta = 0^\circ$  reproduced the same training FEM field when the incoming angle was set to  $\theta = 45^\circ$  and  $-30^\circ$ . In conclusion, we showed numerically that single-realization finite-size SHU arrays feature an isotropic homogenized response to the incoming radiation.

## Conclusions

In this article, we developed and applied the novel framework of multiscale physics-informed neural networks to inversely retrieve the effective dielectric permittivity of finite-size arrays of scattering nanocylinders with stealthy hyperuniform and uncorrelated Poisson geometries. Our results demonstrate that multiscale physics-informed neural networks are capable of accurately capturing the fast-varying spatial variations of complex fields scattered by the investigated arrays, thus enabling a systematic methodology to retrieve their effective dielectric behavior. We demonstrate the existence of a transparency region in finite-size SHU structures beyond the long-wavelength approximation, enabling effective and isotropic homogenization even without disorder-averaging, in contrast to the case of uncorrelated Poisson random patterns. Specifically, we found that the retrieved permittivity distribution  $\hat{\epsilon}(x, y; k)$  obtained for a

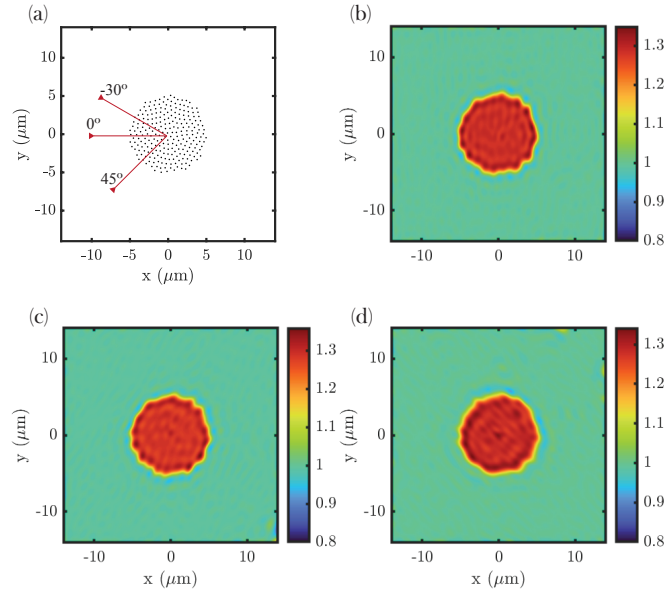


Figure 7: (a) Schematics of the angles employed to study the angular independence in the homogenization of a SHU array of  $N = 236$  particles,  $\chi = 0.5$ ,  $\epsilon_r = 3.0$ ,  $\langle d \rangle / \lambda = 0.09$ , and packing fraction  $\phi = 0.20$ . (b)-(d) MscalePINNs’s reconstruction of the homogenized permittivity profile  $\epsilon_r(x, y)$  retrieved by training on incident light with wavelength  $\lambda = 6.28 \mu\text{m}$  at three different angles:  $\theta = 0^\circ, 45^\circ, -30^\circ$ . The averages of  $\langle \text{Re}[\hat{\epsilon}(x, y; k)] \rangle$  in the homogenized regions agree and show that the homogenization is independent of the angle of incidence.

single-realization of stealthy hyperuniform disorder agrees with the ensemble average calculations with an error close to 1%, whereas a large standard deviation of  $\hat{\epsilon}(x, y; k)$  is obtained for Poisson arrays of comparable sizes. Importantly, we showed that homogenized SHU structures feature isotropic responses to an incoming plane wave excitation that are not appreciably modified by their finite size, which is a highly desired characteristic for the engineering of angle-insensitive photonic media and metamaterials. Moreover, we established through numerous examples that MscalePINN is a necessary powerful extension of traditional single-scale PINN architectures when dealing with multiple scattering contributions in the retrieval of effective medium parameters of complex media. Future work can naturally generalize the multiscale PINN framework introduced here in order to inversely retrieve both the dielectric and the magnetic effective parameters of scattering structures in arbitrary three-dimensional geometries, enabling the inverse design of finite-size resonant nanophotonic devices and metamaterials with desired electromagnetic responses. Lastly, our work provides an efficient route towards the discovery of novel structures with effective medium properties arising from the interaction of disordered scattering geometries and vector or scalar waves of arbitrary nature, including acoustic, mechanical, and quantum wave phenomena.

## Acknowledgments

L. D. N. acknowledges the support from the U.S. Army Research Office, RF-Center managed by Dr. T. Oder (Grant #W911NF-22-2-0158). S. T. acknowledges the support of the U.S. Army Research Office under Cooperative Agreement No. W911NF-22-2-0103. The work of W. Cai is supported by the US National Science Foundation grant DMS-2207449.

## References

- [1] Salvatore Torquato and Frank H. Stillinger. Local density fluctuations, hyperuniformity, and order metrics. *Physical Review E*, 68(4):041113, October 2003. Publisher: American Physical Society.
- [2] Salvatore Torquato. Hyperuniform states of matter. *Physics Reports*, 745:1–95, June 2018.
- [3] Zheng Ma and Salvatore Torquato. Random scalar fields and hyperuniformity. *Journal of Applied Physics*, 121(24):244904, June 2017.
- [4] F. Sgrignuoli, S. Torquato, and L. Dal Negro. Subdiffusive wave transport and weak localization transition in three-dimensional stealthy hyperuniform disordered systems. *Physical Review B*, 105(6):064204, February 2022. Publisher: American Physical Society.
- [5] G. Gkantzounis, T. Amoah, and M. Florescu. Hyperuniform disordered phononic structures. *Physical Review B*, 95(9):094120, March 2017. Publisher: American Physical Society.
- [6] Weining Man, Marian Florescu, Eric Paul Williamson, Yingquan He, Seyed Reza Hashemizad, Brian Y. C. Leung, Devin Robert Liner, Salvatore Torquato, Paul M. Chaikin, and Paul J. Steinhardt. Isotropic band gaps and freeform waveguides observed in hyperuniform disordered photonic solids. *Proceedings of the National Academy of Sciences*, 110(40):15886–15891, October 2013. Publisher: Proceedings of the National Academy of Sciences.
- [7] R. Degl’Innocenti, Y. D. Shah, L. Masini, A. Ronzani, A. Pitanti, Y. Ren, D. S. Jessop, A. Tredicucci, H. E. Beere, and D. A. Ritchie. Hyperuniform disordered terahertz quantum cascade laser. *Scientific Reports*, 6(1):19325, January 2016. Publisher: Nature Publishing Group.
- [8] Haoyang Zhang, Hongchen Chu, Henry Giddens, Wen Wu, and Yang Hao. Experimental demonstration of Luneburg lens based on hyperuniform disordered media. *Applied Physics Letters*, 114(5):053507, February 2019.
- [9] S. Gorsky, W. A. Britton, Y. Chen, J. Montaner, A. Lenef, M. Raukas, and L. Dal Negro. Engineered hyperuniformity for directional light extraction. *APL Photonics*, 4(11):110801, November 2019.
- [10] Salvatore Torquato and Jaek Kim. Nonlocal Effective Electromagnetic Wave Characteristics of Composite Media: Beyond the Quasistatic Regime. *Physical Review X*, 11(2):021002, April 2021. Publisher: American Physical Society.
- [11] Jaek Kim and Salvatore Torquato. Theoretical prediction of the effective dynamic dielectric constant of disordered hyperuniform anisotropic composites beyond the long-wavelength regime [Invited]. *Optical Materials Express*, 14(1):194–215, January 2024. Publisher: Optica Publishing Group.
- [12] Haoyang Zhang, Wen Wu, Qiao Cheng, Qiaoyu Chen, Yin-Hua Yu, and Da-Gang Fang. Reconfigurable Reflectarray Antenna Based on Hyperuniform Disordered Distribution. *IEEE Transactions on Antennas and Propagation*, 70(9):7513–7523, September 2022.
- [13] Marian Florescu, Salvatore Torquato, and Paul J. Steinhardt. Designer disordered materials with large, complete photonic band gaps. *Proceedings of the National Academy of Sciences*, 106(49):20658–20663, December 2009. Publisher: Proceedings of the National Academy of Sciences.
- [14] Wenlong Shi, David Keeney, Duyu Chen, Yang Jiao, and Salvatore Torquato. Computational design of anisotropic stealthy hyperuniform composites with engineered directional scattering properties. *Physical Review E*, 108(4):045306, October 2023. Publisher: American Physical Society.
- [15] Leung Tsang, Jin Au Kong, and Kung-Hau Ding. *Scattering of electromagnetic waves. Theories and applications*. Wiley series in remote sensing. Wiley, New York, 2000.
- [16] Luca Dal Negro. *Waves in complex media: fundamentals and device applications*. Cambridge University Press, New York, 2022.
- [17] Akira Ishimaru. *Wave propagation and scattering in random media*. Academic Press, New York, 1978.

- [18] Zhun Wei and Xudong Chen. Deep-Learning Schemes for Full-Wave Nonlinear Inverse Scattering Problems. *IEEE Transactions on Geoscience and Remote Sensing*, 57(4):1849–1860, April 2019. Conference Name: IEEE Transactions on Geoscience and Remote Sensing.
- [19] Lu Lu, Raphaël Pestourie, Wenjie Yao, Zhicheng Wang, Francesc Verdugo, and Steven G. Johnson. Physics-Informed Neural Networks with Hard Constraints for Inverse Design. *SIAM Journal on Scientific Computing*, 43(6):B1105–B1132, January 2021. Publisher: Society for Industrial and Applied Mathematics.
- [20] M. Raissi, P. Perdikaris, and G. E. Karniadakis. Physics-informed neural networks: A deep learning framework for solving forward and inverse problems involving nonlinear partial differential equations. *Journal of Computational Physics*, 378:686–707, February 2019.
- [21] Lu Lu, Xuhui Meng, Zhiping Mao, and George Em Karniadakis. DeepXDE: A Deep Learning Library for Solving Differential Equations. *SIAM Review*, 63(1):208–228, January 2021. Publisher: Society for Industrial and Applied Mathematics.
- [22] Guofei Pang, Lu Lu, and George Em Karniadakis. fPINNs: Fractional Physics-Informed Neural Networks. *SIAM Journal on Scientific Computing*, 41(4):A2603–A2626, January 2019. Publisher: Society for Industrial and Applied Mathematics.
- [23] Pankaj Mehta, Marin Bukov, Ching-Hao Wang, Alexandre G. R. Day, Clint Richardson, Charles K. Fisher, and David J. Schwab. A high-bias, low-variance introduction to Machine Learning for physicists. *Physics Reports*, 810:1–124, May 2019.
- [24] Yuyao Chen, Lu Lu, George Em Karniadakis, and Luca Dal Negro. Physics-informed neural networks for inverse problems in nano-optics and metamaterials. *Optics Express*, 28(8):11618–11633, April 2020. Publisher: Optica Publishing Group.
- [25] Yuyao Chen and Luca Dal Negro. Physics-informed neural networks for imaging and parameter retrieval of photonic nanostructures from near-field data. *APL Photonics*, 7(1):010802, January 2022.
- [26] R. Riganti and L. Dal Negro. Auxiliary physics-informed neural networks for forward, inverse, and coupled radiative transfer problems. *Applied Physics Letters*, 123(17):171104, October 2023.
- [27] Zhi-Qin John Xu. Frequency Principle: Fourier Analysis Sheds Light on Deep Neural Networks. *Communications in Computational Physics*, 28(5):1746–1767, June 2020.
- [28] Nasim Rahaman, Aristide Baratin, Devansh Arpit, Felix Draxler, Min Lin, Fred Hamprecht, Yoshua Bengio, and Aaron Courville. On the Spectral Bias of Neural Networks. In *Proceedings of the 36th International Conference on Machine Learning*, pages 5301–5310. PMLR, May 2019. ISSN: 2640-3498.
- [29] Jian Cheng Wong, Chinchun Ooi, Abhishek Gupta, and Yew-Soon Ong. Learning in Sinusoidal Spaces with Physics-Informed Neural Networks. *IEEE Transactions on Artificial Intelligence*, pages 1–15, 2022. Conference Name: IEEE Transactions on Artificial Intelligence.
- [30] Basri Ronen, David Jacobs, Yoni Kasten, and Shira Kritchman. The Convergence Rate of Neural Networks for Learned Functions of Different Frequencies. In *Advances in Neural Information Processing Systems*, volume 32. Curran Associates, Inc., 2019.
- [31] Sifan Wang, Hanwen Wang, and Paris Perdikaris. On the eigenvector bias of Fourier feature networks: From regression to solving multi-scale PDEs with physics-informed neural networks. *Computer Methods in Applied Mechanics and Engineering*, 384:113938, October 2021.
- [32] Ziqi Liu, Wei Cai, and Zhi-Qin John Xu. Multi-scale Deep Neural Network (MscaleDNN) for Solving Poisson-Boltzmann Equation in Complex Domains. *Communications in Computational Physics*, 28(5):1970–2001, June 2020. arXiv:2007.11207 [physics].

- [33] Lulu Zhang, Wei Cai Null, and Zhi-Qin John Xu. A Correction and Comments on “Multi-Scale Deep Neural Network (MscaleDNN) for Solving Poisson-Boltzmann Equation in Complex Domains CiCP, 28(5):1970–2001,2020”. *Communications in Computational Physics*, 33(5):1509–1513, June 2023.
- [34] COMSOL AB. COMSOL Multiphysics® v. 6.0, Stockholm, Sweden, 2024.
- [35] Martín Abadi, Ashish Agarwal, Paul Barham, Eugene Brevdo, Zhifeng Chen, Craig Citro, Greg S. Corrado, Andy Davis, Jeffrey Dean, Matthieu Devin, Sanjay Ghemawat, Ian Goodfellow, Andrew Harp, Geoffrey Irving, Michael Isard, Yangqing Jia, Rafal Jozefowicz, Lukasz Kaiser, Manjunath Kudlur, Josh Levenberg, Dandelion Mané, Rajat Monga, Sherry Moore, Derek Murray, Chris Olah, Mike Schuster, Jonathon Shlens, Benoit Steiner, Ilya Sutskever, Kunal Talwar, Paul Tucker, Vincent Vanhoucke, Vijay Vasudevan, Fernanda Viégas, Oriol Vinyals, Pete Warden, Martin Wattenberg, Martin Wicke, Yuan Yu, and Xiaoqiang Zheng. TensorFlow: Large-scale machine learning on heterogeneous systems, 2015. Software available from tensorflow.org.
- [36] Ari H. Sihvola. *Electromagnetic mixing formulas and applications*. Number 47 in IEE electromagnetic waves series. Institution of Electrical Engineers, London, repr. with new cover edition, 2008.